Delft University of Technology

Document Version
Final published version

Licence
Dutch Copyright Act (Article 25fa)

Citation (APA)
Zhao, C., Zhang, W., Zhang, S., Zhang, L., Han, F., Lei, J., Li, Y., & Zhou, W. (2026). Co-regulation of substrate flux and biomass density for enhanced ammonia assimilation under saline conditions. *Bioresource Technology*, *444*, Article 133947. https://doi.org/10.1016/j.biortech.2026.133947

Important note
To cite this publication, please use the final published version (if applicable).
Please check the document version above.

Copyright
In case the licence states “Dutch Copyright Act (Article 25fa)”, this publication was made available Green Open Access via the TU Delft Institutional Repository pursuant to Dutch Copyright Act (Article 25fa, the Taverne amendment). This provision does not affect copyright ownership.
Unless copyright is transferred by contract or statute, it remains with the copyright holder.

Sharing and reuse
Other than for strictly personal use, it is not permitted to download, forward or distribute the text or part of it, without the consent of the author(s) and/or copyright holder(s), unless the work is under an open content license such as Creative Commons.

Takedown policy
Please contact us and provide details if you believe this document breaches copyrights.
We will remove access to the work immediately and investigate your claim.

*This work is downloaded from Delft University of Technology.*

Bioresource Technology 444 (2026) 133947

Contents lists available at ScienceDirect

Bioresource Technology

journal homepage: www.elsevier.com/locate/biortech

# Co-regulation of substrate flux and biomass density for enhanced ammonia assimilation under saline conditions

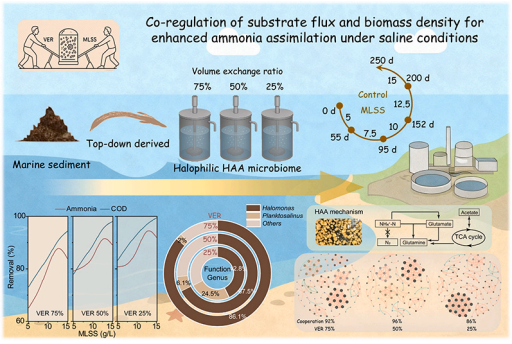
Chuanfu Zhao [a,b], Wenhao Zhang [a,b], Shuhui Zhang [a,b], Lei Zhang [c], Fei Han [a,b], Jianhua Lei [a,b], Yuke Li [d], Weizhi Zhou [a,b,*]

[a] School of Civil Engineering, Shandong University, Jinan, Shandong, PR China
[b] Laboratory of Water-Sediment Regulation and Eco-Decontamination, Jinan, Shandong, PR China
[c] Sinopec Petroleum Engineering Design Co., Ltd, Dongying, Shandong 257026, PR China
[d] Department of Water Management, Faculty of Civil Engineering and Geosciences, Delft University of Technology, Stevinweg 1, 2628 CN Delft, the Netherlands

## HIGHLIGHTS

- Halophilic HAA microbiome is effectively and directionally regulated by VER–MLSS.
- Low VER reduced sludge activity, while excessive VER impaired floc settleability.
- High sludge loading leads to more protein-rich EPS and redox-active functional groups.
- Low sludge loading selectively enriched *Halomonas* and *Marinobacter* as dominant taxa.
- About 50 % VER and 10–12.5 g/L MLSS is optimal load combination for HAA microbiome.

## GRAPHICAL ABSTRACT




## ARTICLE INFO

*Keywords:*
Heterotrophic ammonia assimilation
Volumetric exchange ratio
Mixed liquor suspended solids
High-salinity wastewater treatment

## ABSTRACT

Drawing inspiration from the self-regulating carbon–nitrogen cycling of saline ecosystems, this study investigates how substrate flux and biomass density co-regulate the structure and function of marine sediment-derived halophilic heterotrophic ammonia assimilation (HAA) microbiome cultivated in saline ammonia-containing wastewater with a COD/N radio of 20 under volumetric exchange ratios (VER) of 75 %, 50 %, and 25 % and mixed liquor suspended solids (MLSS) increasing from 5 to 15 g/L. The combined variation in VER and MLSS generated a gradient in food-to-microorganism radio (F/M). With increasing in biomass, COD removal efficiencies peaked at 94.4–99.3 % at 15 g MLSS/L, whereas ammonia removal efficiencies reached at 90.3–96.8 % at 12.5 g MLSS/L before declining. A VER of 25 % reduced sludge activity, while a VER of 75 % impaired floc settleability. The directed HAA community shifted in substrate flux and biomass density, centering on dominant genera such as *Halomonas* and *Marinobacter*, ultimately forming a stable microbiome.

* Corresponding author.
*E-mail address:* wzzhou@sdu.edu.cn (W. Zhou).

https://doi.org/10.1016/j.biortech.2026.133947
Received 16 October 2025; Received in revised form 19 November 2025; Accepted 3 January 2026
Available online 4 January 2026
0960-8524/© 2026 Elsevier Ltd. All rights are reserved, including those for text and data mining, AI training, and similar technologies.

## 1. Introduction

The anthropogenic and natural fluxes of organic carbon and reactive nitrogen across watersheds, estuaries, and continental shelves generate pulsed and chronic resource patterns that fundamentally shape microbiome assembly and biogeochemical function (Bauer et al., 2013). From a large-scale ecological perspective, the principles underlying biological loading optimization parallel nutrient-biomass dynamics observed in estuaries, deltas, and coastal marine ecosystems, where periodic nutrient pulses interact with resident biomass to shape primary production, organic matter turnover, and nitrogen-cycling pathways (Mason-Jones et al., 2023). In these natural systems, excessive nutrient input relative to the biomass capacity often triggers harmful eutrophication or shifts towards undesirable community structures, whereas insufficient nutrient flux may suppress productivity and favor catabolic pathways over biomass synthesis (McDowell et al., 2025). When these principles are translated to engineered systems, it is suggested that an optimal microorganism-sludge loading— a critical but underexplored design variable—exists where substrate flux matches the biomass assimilation capacity, enabling stable, high-efficiency ammonium assimilation without overgrowth or washout (Henry & Bergelson, 2025; Montgomery et al., 2025).

In engineered biological wastewater treatment systems, microorganism sludge loading can be conceptualized as the intersection of two core ecological drivers or operational levers (Chang et al., 2021). Specifically, the volumetric exchange ratio (VER) controls the substrate-input magnitude, periodicity, and hydraulic loading, whereas mixed liquor suspended solids (MLSS) determine the standing biomass and substrate assimilation capacity. These two operational levers map directly onto the aforementioned ecological axes (Henry & Bergelson, 2025) and plays a pivotal role in determining the balance between substrate flux ("food") and biomass density ("eaters") within the ecosystem. A high VER could stimulate heterotrophic activity and ammonia assimilation but risks sludge bulking and settleability deterioration (Al-Mutairi, 2009), whereas high MLSS may intensify endogenous respiration, reduce net nitrogen assimilation efficiency, and lead to energy wastage (Cardete et al., 2017). The food-to-microorganisms ratio (F/M) integrates these parameters, with a low F/M limiting biomass synthesis and a high F/M promoting nitrogen incorporation but potentially destabilizing sludge; thus, optimizing the F/M alongside VER and MLSS provides a unified framework for stable microbial community assembly.

The substrate flux–biomass density balance is especially critical in high-salinity wastewater treatment, where the halophilic microbial community must simultaneously maintain osmotic stability and perform nitrogen removal under conditions that inhibit many conventional freshwater microorganisms (Han et al., 2023b). Halophilic heterotrophic ammonia assimilation processes (HAA) are particularly critical, as they directly incorporate inorganic ammonia into microbial biomass with the assistance of carbon metabolism and the glutamine synthetase-glutamate synthase (GS-GOGAT) pathway, in which ammonia combines with 2-oxoglutarate to form glutamate (Zhang et al., 2021). Ammonia assimilation could result in nitrogen removal without producing nitrite, nitrate, or nitrous oxide, thereby preventing secondary pollution and conserving reactive nitrogen in an organic form, in accordance with circular economy-principles (Zhang et al., 2025b). Most researches on saline wastewater nitrogen assimilation have focused on modulating environmental parameters such as C/N ratio (Zhang et al., 2022), salinity acclimation (Zhao et al., 2024b), or aeration strategies (Zhao et al., 2025). However, how specific regulatory factors as substrate flux and biomass density jointly shape halophilic HAA microbiomes under saline conditions remains unclear. This study hypothesizes that coordinated regulation of VER and MLSS can direct microbial assembly and stabilize metabolic nitrogen assimilation under salinity stress.

Herein, a halophilic microbial community was derived from marine sediments and assembled through a top-down strategy, selectively enriching obligate HAA populations. In our previous study, the COD/N ratio was identified as a key driver in the targeted enrichment of HAA microbiomes, and a COD/N ratio of 20 represented the optimal value that takes into account both the assimilation efficiency and the operational cost (Han et al., 2023a). Building on this foundation, this study shifts from nutrient stoichiometry to kinetic-biomass coupling regulated by sludge loading. By varying the MLSS (5–15 g/L) under different VER conditions (25–75 %), the optimal balance between substrate supply and biomass capacity that sustained high HAA flux while avoiding biomass overgrowth and instability was determined. Through integrated phenotypic, genetic, and ecological analyses, this work sought to establish sludge loading as a central design principle for engineering robust, self-assembled halophilic HAA microbiomes for nitrogen recovery in high-salinity wastewater systems.

## 2. Materials and methods

### 2.1. Microbiome construction and operation

Three 5 L sequencing batch reactors (SBRs), designated R1, R2, and R3, were operated with influent VER of 75 %, 50 %, and 25 %, respectively. Each cycle lasted 24 h and comprised 15 min of filling, 1380 min of aeration, 30 min of settling, and 15 min of decanting. The aeration rate was 1–3 L/min. The three SBRs were operated in parallel across five operational stages with progressively increased MLSS levels (5, 7.5, 10, 12.5, and 15 g/L). Every three days, MLSS concentration was measured, and sludge was withdrawn as necessary to maintain the MLSS at the target level for each stage. The inoculum sludge was sourced from previous study (Han et al., 2023a) and consisted of a salt-tolerant HAA microbial community assembled through a top-down strategy from marine sediments at the station of A4 (123°2′848″ E, 36°0′614″ N) under a simulated wastewater cultivation with COD/N ratio of 20 and a salinity of 3 %.

The salinity of 3 % was chosen because it reflects average seawater and lies within the optimal range for halophilic HAA. Our previous studies showed that very low (0–1 %) or high salinity (>7%) significantly reduces assimilation efficiency (Zhang et al., 2025b), while moderate salinity (1–7 %) produces a unimodal response with peak performance at 2–3 % (Zhao et al., 2024b). "Top-down strategy" refers to constructing microbiomes from natural communities through selective enrichment under defined conditions. "Self-assembled halophilic HAA microbiomes" are communities that autonomously form stable, functionally coordinated consortia under selection pressures such as high salinity and ammonia-rich environments. The main components of the wastewater during the entire long-term operation period (0–250 days) were as follows (mg/L): COD (as NaAc) 2000, $NH_4^+$-N (as $NH_4Cl$) 100, P (as $K_2HPO_4$) 20, NaCl 30000. In batch tests, group I with 30 mg/L allylthiourea (ATU) to suppress potential interference from ammoxidation and group II without ATU were conducted to examine HAA pollutant removal with different MLSS and influent loads, and hourly COD, $NH_4^+$-N and TN biomass/supernatant measurements per (Zhang et al., 2025b). To ensure the scientific validity and reproducibility of the data, the average values were obtained from three parallel samplings and measurements conducted at the same time point.

### 2.2. Analytical methods

The concentrations of COD, TN, $NH_4^+$-N, $NO_2^-$-N, and $NO_3^-$-N were measured following standard APHA method (APHA, 2005). Two-way ANOVA was performed to evaluate the main and interactive effects of MLSS and VER on reactor performance parameters. F/M was calculated as the amount of organic substrate supplied per unit mass of activated sludge per unit time (see Supplementary Materials). Parameters for three-dimensional fluorescence spectroscopy (3D-EEM) analysis with parallel factor analysis (PARAFAC) was based on previous study (Zhao et al., 2024a). Extracellular polymeric substance (EPS) was extracted by

an improved thermal extraction method (Zhao et al., 2023). The contents of protein (PN) and polysaccharide (PS) were determined by anthrone-sulfuric acid method and the modified Lowry method (Zhao et al., 2024a). Functional groups and chemical bonds were analyzed through Fourier Transform infrared spectroscopy (FTIR) using the Thermofisher Nicolet iS 50 instruments (Zhang et al., 2025b). The protein secondary structure was analyzed by the deconvolution fitting of the amide I region of FTIR using Peakfit software (Zhang et al., 2025b). The electrochemical characterization of EPS with an electrochemical workstation (CHI760E, CH Instruments, China), including cyclic voltammetry (CV), linear sweep voltammetry (LSV), differential pulse voltammetry (DPV) and electrochemical impedance analysis (EIS), were based on previous study (Zhang et al., 2025b). Glutamate dehydrogenase (GDH), glutamine synthetase (GS), glutamine synthase (GOGAT), total amino acids (TAA), glutamine (Gln), and glutamate (Glu) in sludge were quantified using corresponding assay kits (Solarbio, Beijing, China) (Zhao et al., 2025). Detailed steps of analytical methods, including EPS extraction, electrochemical testing methods and calculation methods for redox parameters, and enzyme assays, have been added to the Supplementary Materials.

### 2.3. Microbial community analysis

Sludge samples were collected at the end of each stage for high-throughput sequencing analysis using 515F and 806R primers. Bacterial genomic DNA was extracted from the sludge samples using the PowerSoil DNA Separation Kit (MoBio Laboratories, Carlsbad, CA, USA). Sequencing data (raw data) are accessible in the National Center for Biotechnology Information database under accession number PRJNA1257376. Detailed microbial experimental procedures and sequencing methods were provided in the Supplementary Materials. PICRUSt2 was employed to analyze differences in functional genes (Zhao et al., 2024a). In-depth microbial community analysis was applied (see supplementary materials), including microbial networks, network robustness, habitat specialization, neutral community, null model calculations, niche breadth, similarity percentage (SIMPER), Procrustes analysis, mantel analysis, and partial least squares pathway modeling (PLS-PM) (Zhao et al., 2025).

## 3. Results and discussion

### 3.1. Responses of nutrient metabolism to increasing biomass density

In different substrate fluxes (VER 75 %, 50 % and 25 %), HAA was acclimated under a MLSS gradient ranging from 5 g/L to 15 g/L (Fig. 1). In Fig. 1A, effluent $NH_4^+$-N concentrations were substantially reduced with increasing MLSS. The enhancement in $NH_4^+$-N removal was achieved under conditions of higher MLSS and lower VER, while the accumulation of $NO_2^-$-N and $NO_3^-$-N remained negligible (see supplementary materials). At low biomass levels (5 g/L MLSS), $NH_4^+$-N removal was limited, particularly under high VER (75 %), where the average removal efficiency reached only 65.3 %. The efficiencies consistently exceeded 90 % at MLSS $\geq$ 12.5 g/L under VER 25 %. Comparable trends were also observed in COD removal. When MLSS increased from 12.5 g/L to 15 g/L, $NH_4^+$-N removal efficiencies in all three VER decreased moderately (R1:90.3 % to 84.0 %, R2:93.6 % to 89.2 %, R3:96.8 % to 91.9 %), whereas COD removal continued to increase, suggested a threshold behavior of sludge loading in $NH_4^+$-N removal. Excessive sludge competes for the limited carbon resources for other metabolic processes such as respiration, weakening the share of carbon used for nitrogen assimilation.

The two-way ANOVA was conducted to assess the coordinated effects of MLSS and VER on reactor performance (see supplementary materials). Both factors exhibited significant main effects on $NH_4^+$-N and COD removal ($p < 0.001$), with a notable VER − MLSS interaction for COD ($p = 0.0006$). Removal efficiencies increased with MLSS up to 10–12.5 g/L but declined at 15 g/L, indicating diffusion and metabolic limitations. High biomass intensified maintenance metabolism and competition for

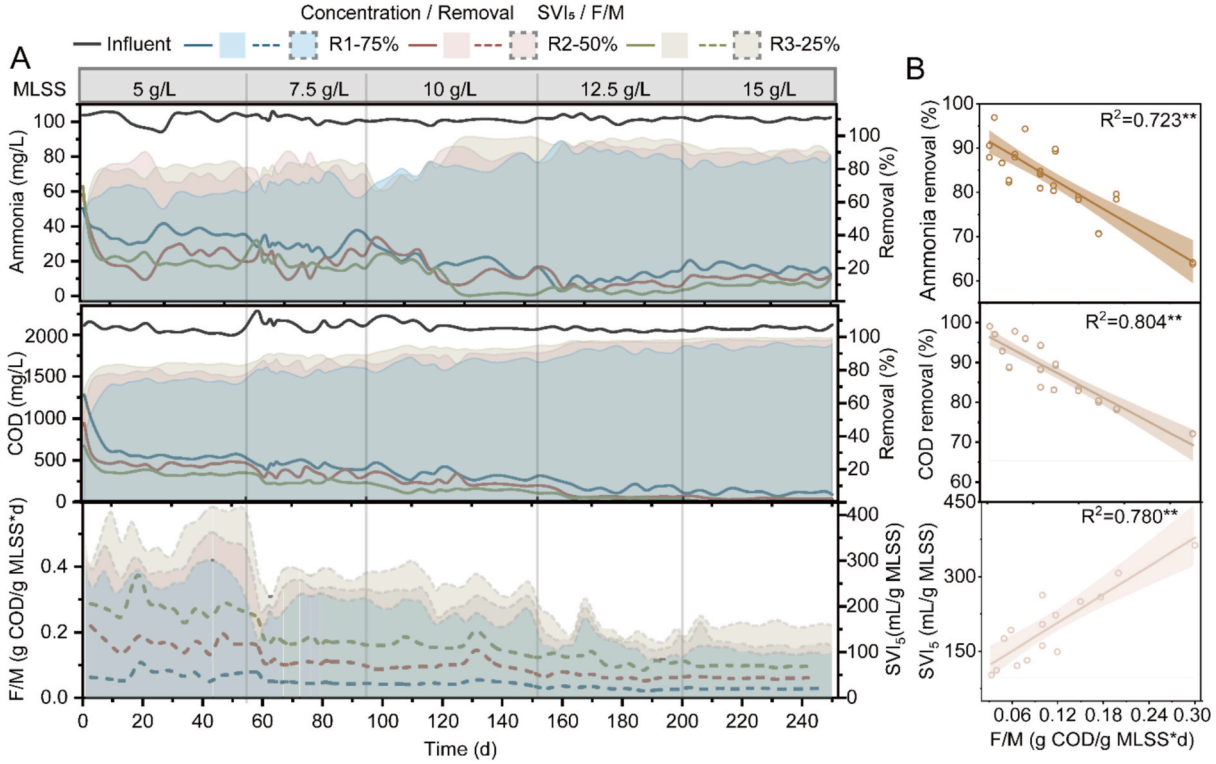



**Fig. 1.** The operational performance of bioreactors with different volume exchange ratios: (A) Pollutant removal performance, the ratio of food to microorganisms (F/M) and the 5-minute sludge volume index ($SVI_5$). (B) Sludge volume index for 5 min ($SVI_5$). Linear correlation analysis of F/M with nitrogen removal, carbon removal and $SVI_5$.

electron acceptors, disrupting the balance between growth and nitrogen assimilation. Thus, both insufficient and excessive MLSS impaired nitrogen uptake, either due to limited biomass (low MLSS) or elevated endogenous respiration (high MLSS).

The carbon and nitrogen mass balance for all reactors across all operational phases were presented in Supplementary materials. At VER 75 %, the nitrogen-based metabolic rate (MR) increased from 1.7 to 2.8 mg N/L* h as MLSS rose from 5 to 12.5 g/L, accompanied by enhanced $NH_4^+$-N removal from 65.3 % to 90.3 %. A similar trend was observed for COD-based MR, which increased from 38.7 to 60.1 mg COD/L*h, reflecting accelerated carbon utilization and HAA under sufficient substrate flux. At VER 50 %, both nitrogen and carbon MR values were moderate (1.2–1.9 mg N/L* h; 22.9–41.5 mg COD/L*h). In contrast, the VER 25 % system exhibited the lowest MR (0.2–0.9 mg N/L* h; 6.1–21.1 mg COD/L*h) despite achieving high overall removal efficiency. When MLSS approached 12.5 g/L, MR plateaued, implying substrate limitation and increased maintenance energy demand. The observed improvement in both $NH_4^+$-N and COD removal was primarily driven by enhanced biomass availability and prolonged substrate contact time. Lower VER effectively reduced the volumetric substrate load per cycle, minimizing substrate shock and providing sufficient residence time for complete assimilation and metabolism. The more pronounced response of $NH_4^+$-N removal to MLSS increments, compared with COD removal, indicated that nitrogen uptake kinetics were particularly dependent on biomass density.

### 3.2. Nitrogen transformation tests of ammonia assimilate microbiome

Batch tests were conducted with and without ATU (30 mg/L) to distinguish the respective contributions of heterotrophic assimilation and nitrification. COD and $NH_4^+$-N concentrations consistently decreased over time under both conditions (see supplementary materials), accompanied by a corresponding increase in biomass-associated TN. In the presence of ATU, the accumulation of $NO_2^-$-N and $NO_3^-$-N was negligible. $NH_4^+$-N removal and biomass TN enrichment proceeded similarly to the ATU-free controls (no significant difference, $p > 0.05$), indicating that HAA was the dominant nitrogen removal pathway (see supplementary materials). COD degradation patterns were unaffected by ATU addition, suggesting that organic carbon was primarily utilized for biomass synthesis rather than respiratory oxidation. With increasing MLSS, both groups with and without ATU maintained nitrogen recovery near 100 %, indicating that ammonium was almost completely converted into biomass nitrogen (see supplementary materials). The C: N coupling ratio gradually decreased, confirming tighter linkage between carbon oxidation and nitrogen assimilation at higher MLSS.

### 3.3. Alternations in operation characteristics analysis of microbiomes

A clear modulation of F/M was achieved by adjusting MLSS concentrations across different operational stages (Fig. 1A). F/M values gradually decreased from 0.30 ± 0.02 g COD/g MLSS·d at 5 g/L MLSS to 0.10 ± 0.01 g COD/g MLSS·d at 15 g/L MLSS for the 75 % VER group, from 0.20 ± 0.03 to 0.067 ± 0.02 g COD/g MLSS·d for the 50 % VER group, and from 0.10 ± 0.05 to 0.033 ± 0.01 g COD/g MLSS·d for the 25 % VER group. The $SVI_5$ values exhibited a significant downward trend as MLSS concentrations increased and F/M values declined. For the 75 % VER group, $SVI_5$ decreased markedly from an average of 362.6 ± 54.1 mL/ g MLSS to 161.0 ± 10.5 mL/g MLSS. Similarly, for the 50 % VER group, $SVI_5$ declined from 306.7 ± 40.7 mL/g MLSS to 120.9 ± 17.8 mL/g MLSS, and for the 25 % VER group, it dropped from 262.5 ± 32.2 mL/g MLSS to 102.2 ± 7.3 mL/g MLSS. Higher biomass concentrations and lower F/M conditions favored the formation of more compact and better-settling flocs. Two-way ANOVA confirmed that both MLSS and VER exerted significant effects on $SVI_5$ ($p < 0.001$), with a marginal interaction ($p = 0.030$), indicating joint control of sludge settleability by biomass density and substrate flux (see supplementary materials).

The correlation between F/M and system performance was further elucidated through regression analysis. In Fig. 1B, significant negative correlations were observed between F/M and nitrogen removal efficiency ($R^2 = 0.723$, $p < 0.01$) and between F/M and carbon removal efficiency ($R^2 = 0.804$, $p < 0.01$). Lower F/M conditions substantially enhanced both nitrogen and carbon removal, likely due to more efficient substrate assimilation and reduced competition among microbial populations. Under moderate or lower F/M, microorganisms were subjected to total amount of nutrients-limited but abundant carbon source conditions, promoting the selection of slow-growing, high-affinity heterotrophs that were typically more efficient in nitrogen assimilation rather than simply increasing the low-nitrogen sludge or consuming carbon sources through respiration. Furthermore, the relationship between F/M and $SVI_5$ was strongly positive ($R^2 = 0.780$, $p < 0.01$). Wang et al. (2023) found that a strong positive linear correlation existed between F/M ratio and SVI. Elevated F/M values were associated with poor sludge settleability (high $SVI_5$), while lower F/M values promoted denser biomass with superior settling properties. This finding reinforced the hypothesis that substrate overload at high F/M encouraged the proliferation of filamentous bacteria or poorly aggregated flocs, leading to bulking phenomena. In contrast, controlled F/M conditions were conducive to stable sludge structure and better hydraulic performance.

### 3.4. Alternations in extracellular polymeric substrates

#### 3.4.1. Fluorescence analysis and polysaccharide − protein contents

The 3D-EEM analysis combined with PARAFAC modeling revealed the fluorescence characteristic changes of EPS released by the microbiomes under different substrate fluxes and biomass densities (Fig. 2A and B and see supplementary materials). Under high VER (75 %), the elevating of biomass concentration (5 to 10 g/L MLSS) lead to the increasing of humic-like (C1) from 43.2 ± 2.1 % to 55.7 ± 3.4 % and the intensifying microbial humification processes. When the MLSS was further increased to 15 g/L, the decline of humus-like (39.3 ± 2.4 %) revealed that substrate limitation or inhibition of humic substance accumulation under excessive biomass loading (Zhang et al., 2025b). Aromatic proteins (*C*2) showed a substantial decline from 46.5 ± 2.9 % to 6.4 ± 0.3 % (5 to 7.5 g/L), followed by a partial recovery at 12.5 g/L (36.1 ± 1.9 %), implying dynamic protein turnover and microbiome shifts (Xie et al., 2025). Fulvic acid-like (C3) and tryptophan-like (C4) generally exhibited low abundance (<25 %), but their peak values under 75 % VER were observed at 7.5 g/L and 15 g/L, respectively, indicating selective release or transformation of intermediate proteinaceous compounds under moderate biomass loads. At medium and low VER (50 % and 25 %), microbial degradation and secondary transformation of SMPs was enhanced. C1 remained dominant at higher MLSS (up to 57.6 ± 2.8 % at 12.5 g/L, 50 % VER), while *C*2 fluctuated strongly, reaching a maximum of 46.5 ± 3.1 % at 7.5 g/L under 25 % VER. Moderate or lower VER conditions favored the accumulation of both humified and protein-like compounds, possibly due to enhanced microbial lysis and limited washout, enabling more complex metabolic processing.

Under high VER (75 %), PN concentrations ranged from 87.8 ± 4.7 to 131.4 ± 6.2 mg/g MLSS as MLSS increased from 5 to 15 g/L (Fig. 2C). The intensified microbial activity and enhanced synthesis of proteinaceous EPS, likely due to increased organic loading and metabolic demand (Lustermans et al., 2025). PS levels remained relatively stable (20.8 ± 0.9–25.8 ± 1.2 mg/g MLSS), resulting in the highest PN/PS ratio of 5.60 ± 0.31 at MLSS 15 g/L. The elevated PN/PS ratio suggested a dominance of PN-rich EPS, potentially favoring flocculation, biofilm formation, and nitrogen assimilation efficiency (Preetham et al., 2025). At medium VER (50 %), similar PN enrichment was observed with increasing MLSS, peaking at 131.2 ± 6.5 mg/g MLSS. Interestingly, PS contents did not decrease substantially, leading to moderate PN/PS ratios (3.30 ± 0.17–5.29 ± 0.24). This balance may support a more stable sludge structure while maintaining sufficient surface reactivity for

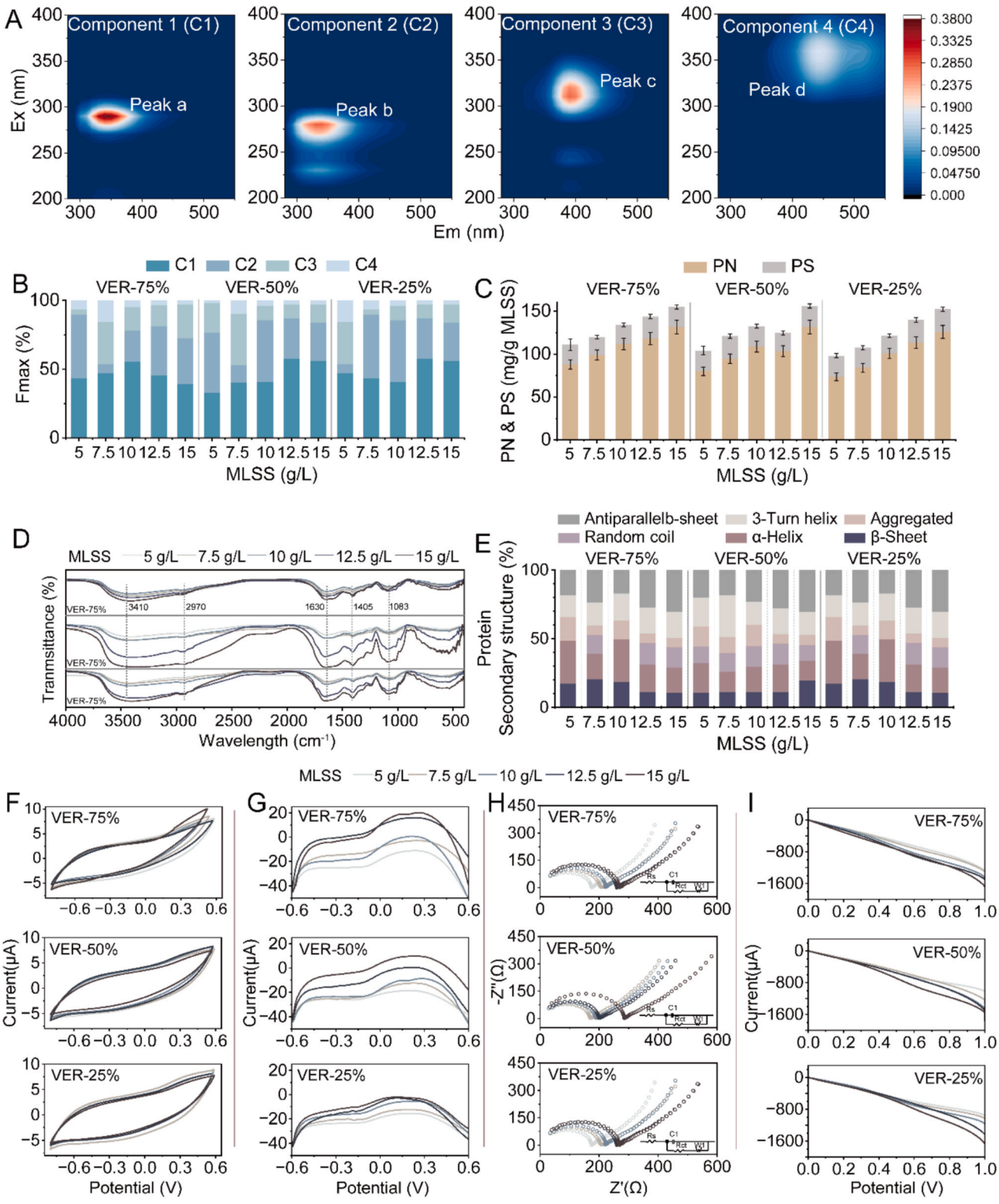



**Fig. 2.** Characterization of extracellular polymeric substances of sludge. Three-dimensional fluorescence spectroscopic analysis: (A) components 1–4 and (B) maximum fluorescence intensity (Fmax). (C) Polysaccharide and protein contents, (D) FTIR spectrograms, and (E) protein secondary structures of EPS. Electrochemical analysis of extracellular polymeric substances of sludge: (F) cyclic voltammetry test (CV), (G) differential pulse voltammetry test (DPV), (H) electrochemical impedance spectroscopy (EIS) and (I) linear cyclic voltammetry test (LSV).

substrate uptake (Yan et al., 2024). Under low VER (25 %), PN levels remained lower at low MLSS (e.g., 73.3 ± 3.8 mg/g MLSS at 5 g/L), but increased sharply to 125.7 ± 6.1 mg/g MLSS at 15 g/L. PS content fluctuated slightly, and PN/PS ratios remained lower at low MLSS (2.96 ± 0.14) but approached values seen in other VER conditions at high MLSS (>4.7). The initially low PN/PS ratio at low MLSS and low VER may indicate reduced microbial secretion activity due to substrate limitation or lower biomass turnover (Wang et al., 2024). The ANOVA

analysis revealed that MLSS and VER exerted significant effects on PN and the PN/PS ratio ($p < 0.001$) (see Supplementary Materials).

### 3.4.2. Protein secondary structures based on FTIR spectrograms

EPS of the microbiomes under different substrate fluxes stimulated by the biomass flux formed the more stable and compact internal structure determined by FTIR spectrum (Fig. 2D). Strong absorption

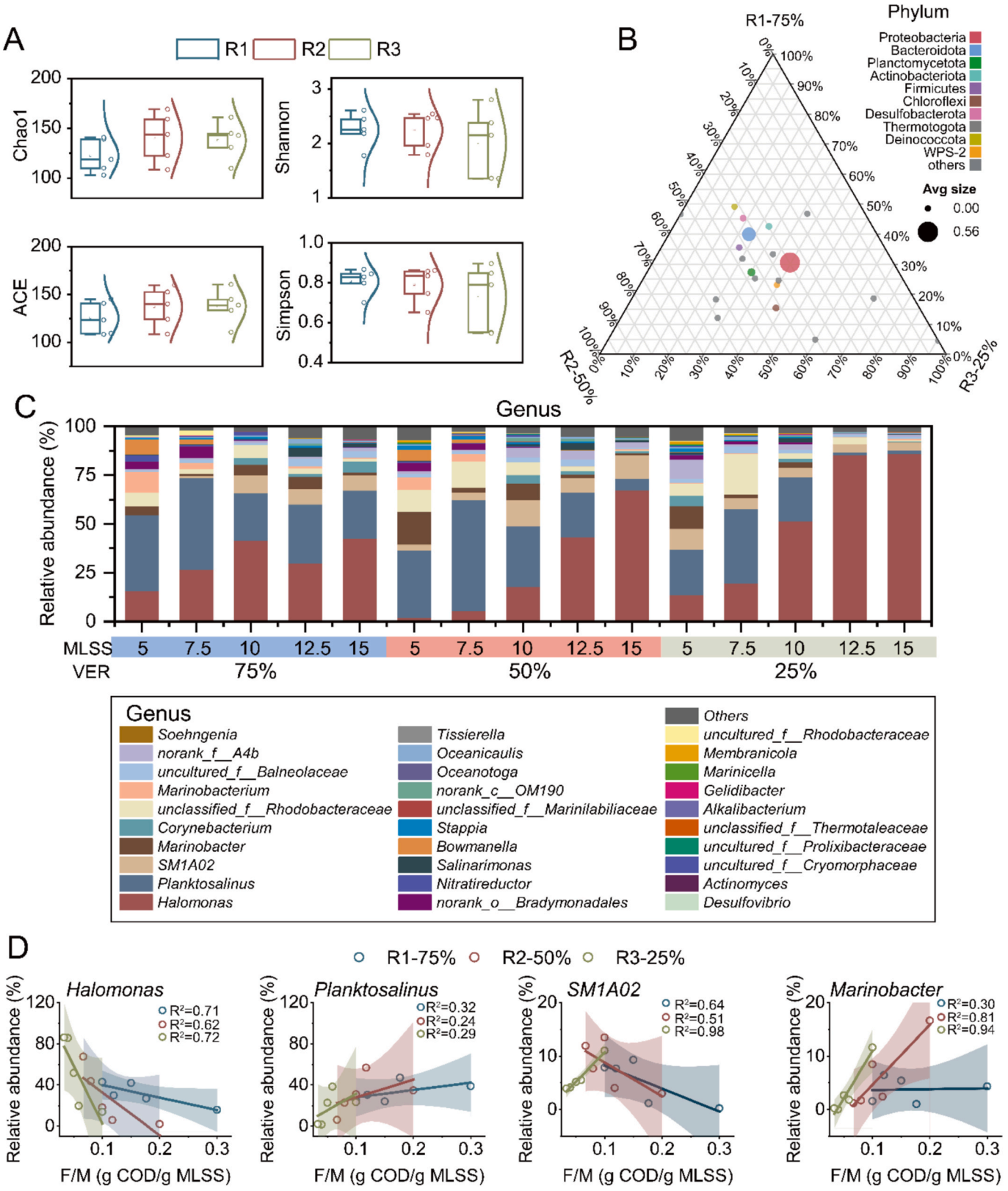



**Fig. 3.** Microbial community: (A) The alpha indices, including chao, sobs, shannon and simpson index. The relative abundance analysis at (B) phyla level and (C) genus level. (D) Linear correlation analysis of dominant microbial genera and F/M.

near 1650 $cm^{-1}$ and 1540 $cm^{-1}$ corresponded to amide I and II regions, signifying prevalent C═O stretching and N—H deformation modes typically associated with proteinaceous components (Zhang et al., 2025b). The broad bands spanning 3200–3400 $cm^{-1}$ pointed to overlapping O—H and N—H stretching, suggestive of hydrogen-bonded hydroxyl and amine functionalities. Vibrations near 1000–1100 $cm^{-1}$, attributed to C—O—C ether linkages and C—O—H bending, highlighted the contribution of polysaccharides. In protein secondary structures in-depth analyzed from amide I region (1600–1700 $cm^{-1}$) (see Supplementary Materials and Fig. 2E), the proportion of α-helix was particularly responsive to the stimulation of substrate fluxes. At high VER (75 %), α-helix content peaked at MLSS 5–10 g/L, suggesting enhanced protein stability favoring nitrogen assimilation, while higher MLSS (12.5–15 g/L) led to increased disordered structures. The ANOVA analysis revealed that α-helix structure exhibited a pronounced interaction effect ($p < 0.001$) (see Supplementary Materials). At moderate VER (50 %), a balanced α-helix/β-sheet profile and elevated 3-turn helix at MLSS 7.5 g/L (30.5 ± 1.6 %) suggested compact, bioactive domains supporting EPS integrity (Zhang et al., 2025b). Under low VER (25 %), α-helix rose sharply at 15 g/L, hinting at compensatory folding, whereas low-MLSS conditions showed more β-sheet aggregates (27.0 ± 1.4 %), implying rigid or denatured protein states (Qin et al., 2025).

### 3.4.3. Electrochemical analysis

More biomass and less influent load led to a decrease in the content of redox-active EPS through electrochemical analyses (Fig. 2F–I). CV indicated that redox activity was maximal at high VER (75 %, R1) with low-moderate MLSS (5–7.5 g/L), showing distinct peaks and high currents (Niu et al., 2024). Increasing MLSS (12.5–15 g/L) reduced peak intensities, suggesting diffusion constraints and lower per-unit electroactivity. Intermediate VER (50 %, R2) showed similar but weaker patterns, while low VER (25 %, R3) yielded nearly flat profiles, reflecting limited EET and recalcitrant EPS accumulation. LSV confirmed maximal anodic currents under R1-5–7.5 g/L, declining at higher MLSS. DPV revealed pronounced oxidation peaks at low MLSS, likely from aromatic groups in active EPS, but peak resolution and intensity diminished at high MLSS, consistent with EPS structural aggregation and reduced electron delocalization (Lustermans et al., 2025). EIS further corroborated these findings, with smallest charge transfer resistance (R_ct) at R1-5 g/L, increasing substantially with MLSS and under lower VERs, indicating hindered electron mobility from dense, resistive EPS layers (Zhang et al., 2025a). Cathodic peak current, peak current from DPV and LSV, and $R_{ct}$ from EIS positively correlate (see Supplementary Materials).

## 3.5. Microbiome response to sludge loading variations

Microbial richness and evenness in alpha indices were found to be modulated by the interaction of VER and MLSS (Fig. 3A). In R1, diversity indices gradually increased from 5 to 12.5 g/L MLSS, with a slight decline at 15 g/L, indicating moderate biomass allowed balanced substrate utilization. R2 showed peak richness at 10–15 g/L but reduced Shannon diversity at extremes, suggesting uneven growth of dominant taxa. In R3, the highest richness occurred at the lowest MLSS, while further biomass increase led to sharp decreases in both Shannon and Simpson indices, reflecting competitive exclusion under excessive microbial density. Two-way ANOVA revealed that VER and MLSS significantly affected all microbial α-diversity indices ($p < 0.001$), confirming their joint regulation of community richness and evenness (see Supplementary Materials). At the phylum level (Fig. 3B), Proteobacteria dominated across all VERs, reflecting their versatile metabolic capacity for HAA and organic carbon utilization, with highest abundance observed in R3 at elevated MLSS, suggesting rapid biomass proliferation under high substrate flux (Schulz-Mirbach et al., 2024). Bacteroidota showed enrichment at moderate MLSS in R1 and R2, consistent with their role in degrading complex organics and supporting nitrogen assimilation through carbon turnover (Zhang et al., 2025c).

At the genus level (Fig. 3C), microbial succession was closely linked to both substrate flux (VER) and biomass density (MLSS). *Halomonas*, a halotolerant heterotroph capable of ammonia assimilation HAA and diverse carbon use (Oren, 2024), increased markedly with MLSS across all VERs, rising from 15.7 % to 42.8 % in R1 (5–15 g/L) and from 1.9 % to 67.5 % in R2. Under low VER (25 %) in R3, *Halomonas* dominated overwhelmingly (>85 %), reflecting its strategist lifestyle with rapid uptake of labile carbon and ammonia via high-affinity transporters and osmoprotectant synthesis that sustain growth under low exchange (Clifton et al., 2024), high biomass-retention environments. *Planktosalinus*, a complex-carbon degrader (Liang et al., 2025), peaked at moderate MLSS (46.9 % at 7.5 g/L in R1; 56.7 % at 7.5 g/L in R2) but declined sharply at higher MLSS, indicating competitive suppression. *SM1A02*, involved in nitrogen transformation and HAA (Chen et al., 2022), expanded from negligible proportions to 9.3 % in R1 (5–10 g/L) and from 3.0 % to 13.5 % in R2, suggesting that intermediate biomass density favored niche occupancy and functional stability. *Marinobacter*, a versatile C/*N*-utilizing genus, exhibited variable trends (Pena-Montenegro et al., 2023), increasing from 4.3 % to 6.4 % in R1 at mid-MLSS but peaking at 16.6 % in R2 at the lowest MLSS, consistent with substrate-limited conditions promoting competitive survival. *Corynebacterium,* capable of HAA (Montgomery et al., 2025), emerged at 3.3 % in R1 and 4.4 % in R2 at intermediate MLSS (10 g/L), reflecting growth under balanced substrate flux and biomass density. *Unclassified* R*hodobacteraceae*, linked to C/N turnover (Pontiller et al., 2022), decreased in R1 from 7.0 % to 1.5 % at high MLSS, while in R3 it reached 20.9 % at moderate MLSS, illustrating differential niche adaptation driven by VER. *Marinobacterium*, a heterotrophic C/N/P-assimilating genus (Lockwood et al., 2022), declined in R1 from 10.6 % to 0.5 % with increasing MLSS, emphasizing competitive exclusion at high biomass. *Bowmanella* and *Stappia*, versatile carbon degraders with denitrification potential (Christie-Oleza et al., 2017), thrived at low-moderate MLSS but were suppressed at high biomass densities due to intensified competition and diffusion limitation.

Genus-level responses revealed nuanced mechanistic interactions between substrate flux, biomass density, and metabolic specialization (Fig. 3D). *Halomonas* abundance exhibited strong negative correlations with F/M across R1–R3 (r = −0.79 to −0.85), reflecting that high F/M conditions—where substrate supply exceeded microbial processing capacity—likely induced metabolic bottlenecks or competitive suppression, whereas moderate F/M allowed exploitation of ammonia and labile carbon with maximal growth efficiency. *Planktosalinus* demonstrated weak positive correlations (r = 0.48–0.57), indicating selective advantage under moderate substrate flux that supported complex polysaccharide degradation without triggering overgrowth of dominant fast-utilizers. *Marinobacter* showed minimal F/M sensitivity in R1 but strong positive correlations in R2-R3 (r = 0.90–0.97), consistent with preferential proliferation under substrate-limited conditions that couple carbon and nitrogen uptake efficiency with available flux.

## 3.6. Microbiome assembly under different substrate flux

In the co-occurrence networks (Fig. 4A), R1 exhibited a high proportion of positive correlations (91.56 %) and strong modularity (0.855), with cooperative clusters dominated by *Halomonas*, *Proteiniclasticum*, and *SM1A02*, indicating synergistic carbon and nitrogen turnover under high VER. Negative correlations (8.44 %) may be related to the niche overlap between *Halomonas* and *Planktosalinus*, reflecting substrate competition in carbon-rich conditions. R2 displayed the highest positive correlation ratio (96.47 %) and balanced modular distribution, with cooperative interactions between *Halomonas*, *Marinobacter*, and *SM1A02* reinforced by cross-module connectors (e.g., *Pseudoalteromonas*, *Hyphomonas*), and minimal competition (3.53 %), supporting functional redundancy and stability under intermediate VER and biomass density. R3, despite having the highest connectivity

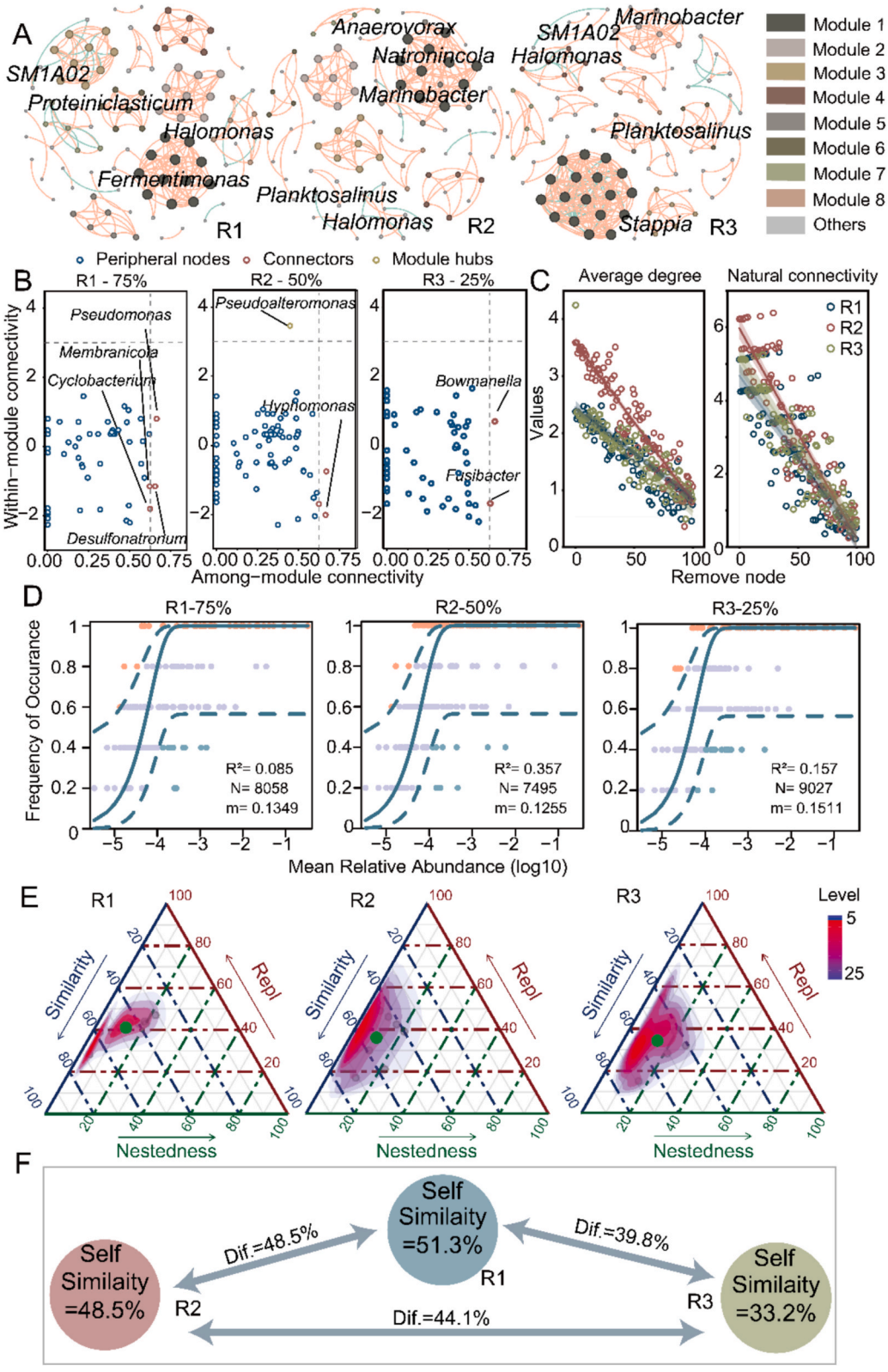



**Fig. 4.** In-depth analysis of microbial communities: (A) Microbiome co-occurrence network. (B) The Z-P plot of species topological roles based on the average degree and natural connectivity. (C) Robustness analysis. (D) Fit of neutral community model (NCM) of community assembly. (E) Triangular plots show community ecological processes (i.e., species substitution and richness differences) of bacteria in the four bioreactors. Its position is denoted by a triplet of values from the Similarity = 1–dissimilarity, Repl (replacement), Nestedness; each triplet sums to 1. (F) Similarity Percentage (SIMPER) of microbial communities.

(average degree 5.86) and edge number (n = 293), showed reduced modularity (0.706) and elevated negative correlations (15.02 %), with dominant *Halomonas* forming extensive positive linkages within its guild but engaging in strong competitive exclusion against *Planktosalinus* and *Bowmanella*, indicating that low VER with high biomass retention favors monopolization by fast-growing taxa at the expense of guild diversity.

Strong correlations of microbiome co-occurrence network findings and functional gene expression indicated that VER-MLSS interactions drive the formation of complex and functionally coupled microbial networks (see Supplementary Materials).

The Z-P plot (Fig. 4B) revealed functional stability supported by both module connectors (*Pseudoalteromonas*, *Hyphomonas*) and module hubs in R2, enabling cross-module resource exchange; R3 lacked such connectors, limiting functional redundancy. Robustness analysis (Fig. 4C) confirmed highest tolerance of R2 to node removal, consistent with redundant pathways and cooperative cross-feeding, whereas R3 degraded sharply upon hub loss. The neutral community model (Fig. 4D) fit was highest for R2 ($R^2 = 0.357$), suggesting equilibrium between selection and stochastic drift; R1 showed low fit (0.085) under strong directional selection; R3′s intermediate fit (0.157) reflected hub-driven stochasticity constrained by deterministic dominance. Ecological process partitioning (Fig. 4E) positioned R2 close to the similarity axis with low replacement and moderate nestedness, indicating deterministic filtering with niche complementarity; the community of R1 was driven by high genera replacement under fluctuating substrate flux, while R3 combined high replacement and nestedness, reflecting niche compression and habitat homogenization. SIMPER analysis (Fig. 4F) highlighted the intermediate taxonomic turnover and balanced contributions of R2 from multiple genera, contrasting with dominance of R1 by fast-growing taxa and uneven of R3 by slow-growing taxa, hub-skewed contributions.

### 3.7. Assimilation metabolism under regulation of biomass density-substrate flux

In Fig. 5A, HAA was supported by distinct patterns of enzyme activity and amino acid accumulation under varying VER-MLSS conditions. GOGAT exhibited the highest activity (759.3 ± 40.6–921.6 ± 46.1 U/g MLSS), indicating its central role in glutamate synthesis (Zhang et al., 2025b), while GDH activity (21.5 ± 1.1–27.9 ± 1.4 mU/g MLSS) showed moderate variation. GS activity remained comparatively low (9.9 ± 0.6–17.6 ± 0.9 U/g MLSS). Glutamine (18.7 ± 0.9–21.7 ± 1.3 mg/g MLSS) and glutamate (17.2 ± 1.0–28.2 ± 1.7 mg/g MLSS) were maintained at stable levels in R2, consistent with balanced nitrogen assimilation and reduced metabolic stress. In contrast, R1 exhibited transient glutamate surges at moderate MLSS, whereas R3 showed declining GOGAT activity and amino acid yields at high MLSS, implying substrate limitation and impaired assimilation efficiency. TAA remained highest in R1 (up to 235.1 ± 11.3 mg/g MLSS) but displayed greater fluctuation, whereas R2 maintained stable TAA (~225 ± 12.6 mg/g MLSS), suggesting that intermediate VER-MLSS coupling favored steady-state amino acid biosynthesis and stable assimilation microbiome function.

KEGG inference revealed an assimilation-dominated nitrogen strategy (Fig. 5B): nitrification markers were absent (*amoA*, *hao* ≈ 0), whereas the GS-GOGAT and GDH pathways achieved absolute dominance. The relative abundance of *glnA* corresponding to the GS pathway, increased with biomass, peaking at R2-15 g/L (0.1852 %) and R3-12.5/15 g/L (0.1993–0.1979 %). In contrast, *gltD*, associated ~~to~~ with the GOGAT pathway, peaked at intermediate MLSS (R2-7.5 g/L, 0.0863 %; R3-7.5 g/L, 0.0846 %) but declined at high MLSS, while *gltB* increased toward later stages (R2-15 g/L, 0.0507 %; R3-12.5/15 g/L, 0.0511–0.0506 %). The ammonium/glutamate transporter *gltS* peaked at moderate MLSS (R2-7.5 g/L, 0.0578 %; R1-7.5 g/L, 0.0565 %) but collapsed at high MLSS (R2-15 g/L, 0.0049 %; R3-15 g/L, 0.0023 %), indicating diffusion or uptake limitations under dense biomass conditions (Han et al., 2023a). *gdhA*, representing the GDH pathway, was elevated at mid-MLSS (R2-7.5 g/L, 0.0803 %; R3-7.5 g/L, 0.0838 %) and decreased thereafter, whereas *GLUD* showed transient increase during early R3 (0.0298–0.0278 %) before declining at high MLSS (0.0046 %). Carbon metabolism and TCA cycle genes supported the supply of carbon skeletons and energy required for nitrogen assimilation. *ACO2* increased with MLSS, reaching its highest levels in R2-15 g/L (0.1001 %) and R3-12.5/15 g/L (0.1004–0.1015 %); *IDH3A* intensified in late stages, especially in R3-12.5/15 g/L (0.0352–0.0353 %). Downstream dehydrogenases (*OGDH*, *SDH*, *FH*) declined with increasing MLSS, implying throttling of deep TCA flux and preferential allocation of α-ketoglutarate to HAA rather than full oxidation.

Genus-gene correlations (Fig. 5B) indicated that *Halomonas* was positively correlated with *glnA*, *gltB/D* and early-TCA nodes (*ACO2*, *IDH3A*), consistent with utilization of the high-affinity GS-GOGAT pathway when substrate flux was limited (notably in R3). *Planktosalinus* aligned with acetate entry (*ackA*) and citrate synthase (*CS*), reflecting coupling between polymer hydrolysate fermentation to TCA cycle entry under moderate metabolic flux (R1-R2). *SM1A02* correlated with GOGAT (*gltB/D*) under low VER, consistent with its specialization in slow-turnover nitrogen specialization (Chen et al., 2022). *Marinobacter* was associated with respiratory dehydrogenases (*DLD*, *SDH*), consistent with flexible C/N respiration at mid-low F/M (R2-R3). *Corynebacterium* was linked to GDH (*gdhA/GLUD*), supporting glutamate anabolism at intermediate MLSS. In conclusion, the GS-GOGAT core pathway operates efficiently at intermediate VER/MLSS was well supplied by upstream TCA steps and supported by complementary microbial genera. In contrast, extreme in VER/MLSS suppressed transport capacity (*gltS*) or overconcentrated flux, thereby undermining stable HAA. Moreover, Procrustes analysis (Fig. 5C) showed that the left-side nitrogen genes cluster closely with associated genera, and right-side carbon genes align with their respective taxa, underscoring strong C—N metabolic coupling and the coordinated microbial functional niches.

In Fig. 5E, KEGG-based enzyme abundances, integrated with the pathway topology in Fig. 5D, revealing sequential coupling of nitrogen and carbon metabolism under varying VER and MLSS. Key C—N interface enzymes, such as EC 2.3.1.9 (acetyl-CoA C-acetyltransferase) and EC 6.3.1.2 (glutamate-ammonia ligase), exhibited progressive increases from low to optimal MLSS, particularly in R2 and R3, indicating enhanced HAA and provision of carbon skeletons. Upstream carbon-related enzymes (EC 4.2.1.3, EC 2.3.1.61) showed higher activities at intermediate MLSS, ensuring a steady supply of intermediates for amino acid biosynthesis (Zhang et al., 2025b). Nitrogen-related enzymes (EC 1.4.1.2, EC 1.4.1.4) significantly increased at higher MLSS in R3, suggesting intensified glutamate-glutamine turnover under reduced substrate flux. In contrast, extremely high MLSS or low VER led to declines in key carbon entry-point enzymes (EC 2.7.2.1, EC 4.2.1.2), reflecting potential metabolic bottlenecks. This dynamic coordination indicates that balanced VER and MLSS sustain robust connectivity across C—N pathway, preventing enzyme activity collapse and maintaining a stable HAA microbiome.

In the PLS-PM (Fig. 5F), functional microbial assemblages were modeled as antecedent drivers of carbon and nitrogen gene modules, with strong positive paths to carbon metabolism and a direct, dominant path from the GS-GOGAT axis to nitrogen assimilation. Carbon-route enzymes (*ACO2*, *CS*) exerted indirect effects on assimilation by supplying α-ketoglutarate and reducing equivalents. Moderate EPS production strengthened C—N coupling by stabilizing microhabitats and promoting cross-feeding interactions. Dense EPS matrices increase diffusion resistance not only for ammonium but also for dissolved oxygen, low-molecular-weight organic carbon, and micronutrients, thereby reducing their effective concentrations at the cell surface. Reciprocal negative feedbacks from accumulated amino acids to upstream transport/gene expression were detected, indicating homeostatic buffering within optimally coupled VER-MLSS regimes.

### 3.8. Prospect

Halophilic HAA process exhibited strong scalability and practical potential for treating high-salinity and high carbon-to-nitrogen (C/N) ratio wastewaters, such as those from petrochemical, food, and landfill leachate sources. Its core advantage lies in its high salt tolerance, strong resistance to shock loads, occupy a compact carbon footprint due to high

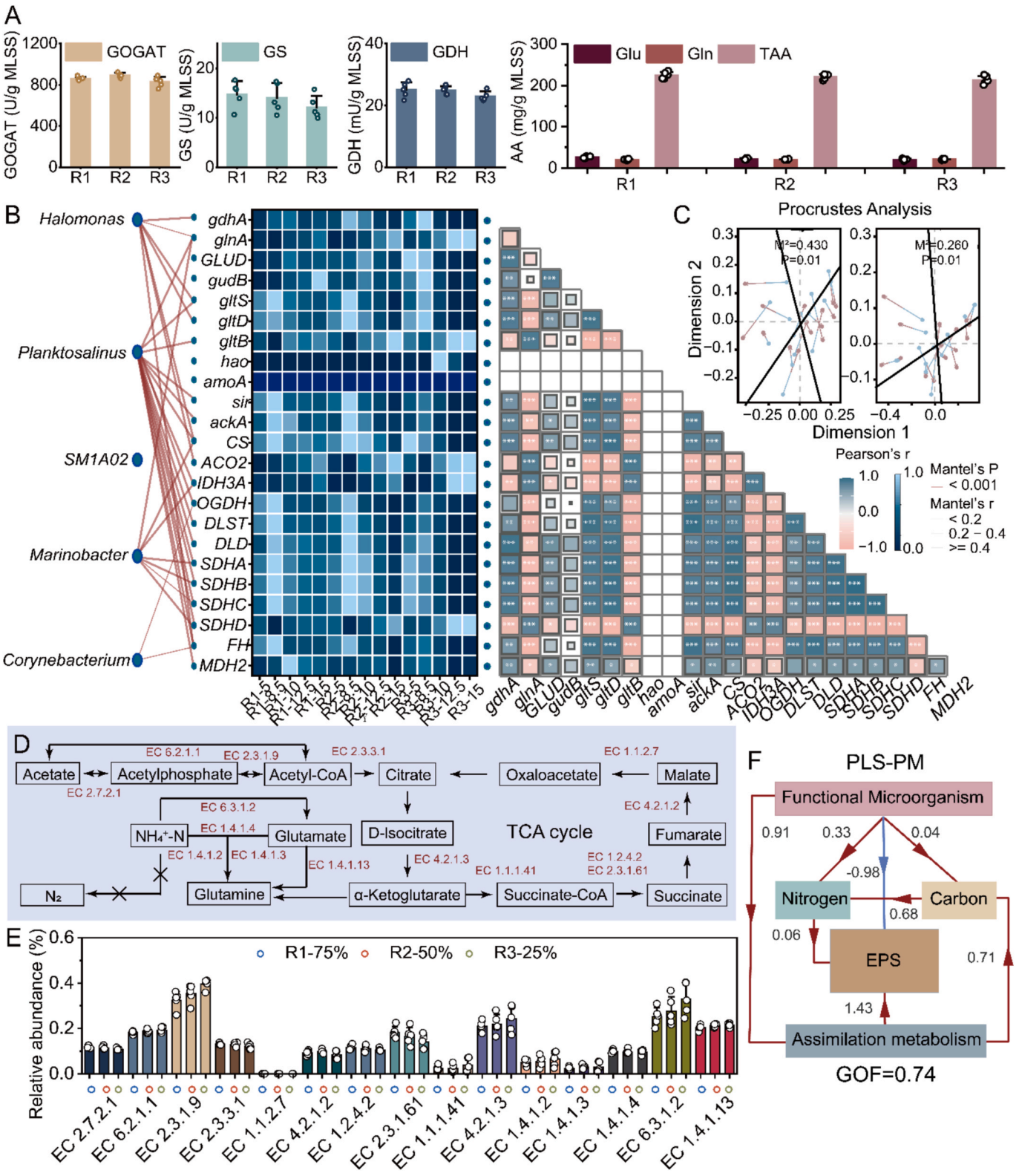



**Fig. 5.** Mechanism analysis: (A) The enzyme activity and amino acids of assimilation pathways. (B) The relative abundances and mental test of the nitrogen and carbon genes and functional microorganisms. (G) Procrustes analysis. (C) Mechanism diagram. (E) Enzyme activity of the nitrogen and carbon cycle predicted by PICRUSt. (F) Partial least-squares path model (PLS-PM) of relationships between functional microorganism, nitrogen, carbon, EPS, and assimilation mechanism (Protein).

biomass yield and retention, and efficient simultaneous removal of carbon and nitrogen through biomass synthesis, rather than oxidation–reduction pathways. In integrated configurations, HAA can be coupled with anaerobic or aerobic carbon-removal units, serving as a stable front-end process, or combined in series or parallel with low-C/N bioreactors, or anammox for biological phosphorus removal and

tailwater treatment. Furthermore, the generated biomass offers potential for valorization as protein-rich material or fertilizer, enhancing overall resource recovery.

## 4. Conclusions

Controlled adjustment of volumetric exchange ratio and biomass concentration was shown to enhance stable halophilic HAA in saline wastewater. Optimal sludge loading (50 % VER, 10~12.5 g/L MLSS) maximized nitrogen removal (>90 %) through the assimilation pathway without nitrification, improved settleability, and enriched protein-rich EPS favorable. Excessive biomass impaired assimilation efficiency, revealing a threshold effect. Dual-lever regulation selectively enriched active HAA populations, such as *Halomonas*, *Marinobacter*, and *Pseudoalteromonas*, collectively contributing to nitrogen assimilation and EPS production. From an engineering perspective, the coordinated regulation of VER and MLSS provided a stable operational window (VER 50 %, MLSS 10–12.5 g/L) that maximized HAA without compromising COD removal, highlighting its applicability for treating saline wastewaters such as oilfield produced water or high-salt landfill leachate. Coordinated VER-MLSS regulation facilitated the stable establishment of a high-rate HAA microbiome and enhances nitrogen assimilation efficiency in saline environments.

## CRediT authorship contribution statement

**Chuanfu Zhao:** Writing – original draft, Data curation. **Wenhao Zhang:** Data curation. **Shuhui Zhang:** Data curation. **Lei Zhang:** Supervision. **Fei Han:** Data curation. **Jianhua Lei:** Data curation. **Yuke Li:** Supervision. **Weizhi Zhou:** Writing – review & editing, Supervision, Project administration, Funding acquisition.

## Declaration of competing interest

The authors declare that they have no known competing financial interests or personal relationships that could have appeared to influence the work reported in this paper.

## Acknowledgments

This work was supported by National Natural Science Foundation of China (92575109); National Key Research and Development Program (2022YFC2807503).

## Appendix A. Supplementary data

Supplementary data to this article can be found online at https://doi.org/10.1016/j.biortech.2026.133947.

## Data availability

Data will be made available on request.

## References

Al-Mutairi, N.Z., 2009. Aerobic selectors in slaughterhouse activated sludge systems: a preliminary investigation. Bioresour. Technol. 100 (1), 50–58.
APHA, 2005. Standard Methods for the Examination of Water and Wastewater. American Public Health Association/American Water Works Association/Water Environment Federation, Washington.
Bauer, J.E., Cai, W.J., Raymond, P.A., Bianchi, T.S., Hopkinson, C.S., Regnier, P.A., 2013. The changing carbon cycle of the coastal ocean. Nature 504 (7478), 61–70.
Cardete, M.A., Mata-Álvarez, J., Dosta, J., Nieto-Sánchez, R., 2017. Influence of hydraulic retention time, food-to-microorganism ratio and influent biodegradability on the performance of an aerobic selector treating petrochemical wastewater. J. Environ. Chem. Eng. 5 (5), 5033–5042.
Chang, C.-Y., Vila, J.C., Bender, M., Li, R., Mankowski, M.C., Bassette, M., Borden, J., Golfier, S., Sanchez, P.G.L., Waymack, R., 2021. Engineering complex communities by directed evolution. Nat. Ecol. Evol. 5 (7), 1011–1023.
Chen, Y.J., Leung, P.M., Cook, P.L.M., Wong, W.W., Hutchinson, T., Eate, V., Kessler, A. J., Greening, C., 2022. Hydrodynamic disturbance controls microbial community assembly and biogeochemical processes in coastal sediments. ISME J. 16 (3), 750–763.
Christie-Oleza, J.A., Sousoni, D., Lloyd, M., Armengaud, J., Scanlan, D.J., 2017. Nutrient recycling facilitates long-term stability of marine microbial phototroph-heterotroph interactions. Nat. Microbiol. 2, 17100.
Clifton, B.E., Alcolombri, U., Uechi, G.I., Jackson, C.J., Laurino, P., 2024. The ultra-high affinity transport proteins of ubiquitous marine bacteria. Nature 634 (8034), 721–728.
Han, F., Zhang, M., Li, Z., Liu, Z., Han, Y., Li, Y., Zhou, W., 2023a. Self-assembly of ammonium assimilation microbiomes regulated by COD/N ratio. Chem. Eng. J. 455, 140782.
Han, F., Zhao, C., Zhang, W., Jiao, T., Zhang, Z., Zhou, W., 2023b. Responses of halophilic microbial communities to changes in salt composition: comparison between autotrophic nitrification and heterotrophic ammonia assimilation biosystems. Bioresour. Technol. 386, 129500.
Henry, L.P., Bergelson, J., 2025. Applying ecological principles to microbiome engineering. Nat. Microbiol. 10 (9), 2111–2121.
Liang, H.K., Cui, Y.W., Yan, H.J., Li, Z.Y., 2025. Recovery of disintegrated halophilic aerobic granular sludge through ferric ion addition: dual roles in filamentous fungal inhibition and microbial adhesion enhancement. Water Res. 283, 123844.
Lockwood, S., Greening, C., Baltar, F., Morales, S.E., 2022. Global and seasonal variation of marine phosphonate metabolism. ISME J. 16 (9), 2198–2212.
Lustermans, J.J.M., Basu, N., Digel, L., Aiyer, K., 2025. Iron reduction under oxic conditions by Microbacterium deferre sp. nov. A1-JK(T). Nat. Commun. 16 (1), 6183.
Mason-Jones, K., Breidenbach, A., Dyckmans, J., Banfield, C.C., Dippold, M.A., 2023. Intracellular carbon storage by microorganisms is an overlooked pathway of biomass growth. Nat. Commun. 14 (1), 2240.
McDowell, R.W., Luo, D., Pletnyakov, P., Upsdell, M., Dodds, W.K., 2025. Anthropogenic nutrient inputs cause excessive algal growth for nearly half the world's population. Nat. Commun. 16 (1), 1830.
Montgomery, A., Zhuang, G.-C., Zhou, Z., Langwig, M.V., Millán-Motolinía, M.d.C., Choi, H.Y.L., Hunter, K.S., Mortera-Gutiérrez, C.A., Hyacinthe, C., Marinelli, Z., Anantharaman, K., Teske, A., Joye, S.B., 2025. Elevated heterotrophic activity in Guaymas Basin hydrothermal plumes influences deep-sea carbon cycling. Nat. Commun. 16 (1), 4934.
Niu, Y., Xue, D., Dai, X., Guo, G., Yang, X., Yang, L., Bai, Z., 2024. Sustainable power generation from sewage with engineered microorganisms as electrocatalysts. Nat. Sustain. 7 (9), 1182–1189.
Oren, A., 2024. Novel insights into the diversity of halophilic microorganisms and their functioning in hypersaline ecosystems. NPJ Biodivers. 3 (1), 18.
Pena-Montenegro, T.D., Kleindienst, S., Allen, A.E., Eren, A.M., McCrow, J.P., Sanchez-Calderon, J.D., Arnold, J., Joye, S.B., 2023. Species-specific responses of marine bacteria to environmental perturbation. ISME Commun. 3 (1), 99.
Pontiller, B., Martinez-Garcia, S., Joglar, V., Amnebrink, D., Perez-Martinez, C., Gonzalez, J.M., Lundin, D., Fernandez, E., Teira, E., Pinhassi, J., 2022. Rapid bacterioplankton transcription cascades regulate organic matter utilization during phytoplankton bloom progression in a coastal upwelling system. ISME J. 16 (10), 2360–2372.
Preetham, V., Singh, A., Tiwary, C.S., Gupta, A.K., 2025. Advancing anammox pathways for wastewater treatment: a focus on conventional carrier challenges and innovations of 3D printed biocarrier. J. Environ. Chem. Eng. 13 (3), 116411.
Qin, W., Li, R., Liu, J., Liu, J., Wang, X., Hu, B., Zheng, Z., Yu, Z., Li, G., 2025. Spatially constrained disulfide bond shuffling delays insulin aggregation and enhances neurotoxicity. Nat. Commun. 16 (1), 6841.
Schulz-Mirbach, H., Wichmann, P., Satanowski, A., Meusel, H., Wu, T., Nattermann, M., Burgener, S., Paczia, N., Bar-Even, A., Erb, T.J., 2024. New-to-nature CO(2)-dependent acetyl-CoA assimilation enabled by an engineered B(12)-dependent acyl-CoA mutase. Nat. Commun. 15 (1), 10235.
Wang, B., Dou, Y., Liang, C., Liu, C., Ao, D., Yao, H., Yang, E., An, S., Wen, Z., 2024. Microbial necromass in soil profiles increases less efficiently than root biomass in long-term fenced grassland: effects of microbial nitrogen limitation and soil depth. Sci. Total Environ. 956, 177058.
Wang, Q., Lin, Y., Peng, L., Wang, Y., Ma, S., Ren, H., Xu, K., 2023. Weak magnetic field enhances waste molasses-driven denitrification during wastewater.
Xie, X., Li, J., Xu, M., Wei, Z., Zhang, S., Zhang, X., Chen, A., Zhang, X., 2025. Regulation of cold-adapted genes by material turnover in low-temperature composting. Chem. Eng. J. 512, 162572.
Yan, L., Miao, J., Ma, Y., Yin, M., Song, X., 2024. Removal of nitrate nitrogen by aerobic denitrification granular sludge under strongly alkaline conditions: performance and mechanism. Chem. Eng. J. 500, 157153.
Zhang, B., Qi, B., Shi, W., Huang, S., Xu, W., Yan, P., Zhang, B., Lens, P.N.L., Peng, Y., 2025a. Impaired denitrification of aerobic granules in response to micro/nanoplastic stress: insights from interspecies interactions and electron transfer processes. Water Res. 279, 123472.
Zhang, M., Han, F., Li, Y., Liu, Z., Chen, H., Li, Z., Li, Q., Zhou, W., 2021. Nitrogen recovery by a halophilic ammonium-assimilating microbiome: a new strategy for saline wastewater treatment. Water Res. 207, 117832.
Zhang, M., Han, F., Liu, Z., Han, Y., Li, Y., Zhou, W., 2022. Ammonium-assimilating microbiome: a halophilic biosystem rationally optimized by carbon to nitrogen ratios with stable nitrogen conversion and microbial structure. Bioresour. Technol. 350, 126911.
Zhang, M., Zhao, C., Zhang, W., Guo, Y., Han, F., Li, Y., Zhou, W., 2025b. Stable ammonium assimilation mediates the metabolic adaptation of halophilic

microbiome to hypo-osmotic stress in wastewater treatment. Water Res. 288, 124572.
Zhang, Z., Liu, Y., Zhao, W., Liu, K., Chen, Y., Wang, F., Mao, G., Ji, M., 2025c. Distinct genes and microbial communities involved in nitrogen cycling between monsoon- and westerlies-dominated Tibetan glaciers. Nat. Commun. 16 (1), 5926.
Zhao, C., Jiao, T., Zhang, W., Guo, Y., Han, F., Lei, J., Zhou, W., 2024a. Carbon sources influence on heterotrophic ammonia assimilation: performance and mechanism. Chem. Eng. J. 497, 154545.
Zhao, C., Jiao, T., Zhang, W., Zhang, W., Jia, M., Liu, S., Zhang, M., Han, F., Han, Y., Lei, J., Wang, X., Zhou, W., 2024b. Nutrients recovery by coupled bioreactor of heterotrophic ammonia assimilation and microbial fuel cell in saline wastewater. Sci. Total Environ. 918, 170697.
Zhao, C., Wang, Y., Meng, S., Zhang, W., Zhang, X., Yan, L., Wei, Q., Wei, D., 2023. Solid slow-release carbon source assembled microbial fuel cell for promoting superior nitrogen removal in an aerobic granular sludge bioreactor. J. Environ. Manage. 325, 116430.
Zhao, C., Zhang, W., Lei, J., Han, F., Zhang, M., Guo, Y., Li, Y., Zhou, W., 2025. UV-activated peroxymonosulfate assisted heterotrophic ammonium assimilation for high-salinity leachate treatment: mechanism and performance evaluation. Environ. Res. 285, 122481.